Nano Research 2014, 7(10): 1528–1547
DOI 10.1007/s12274-014-0514-z
Research Article

ISSN 1998-0124
CN 11-5974/O4

Self-assembly of nitrogen-doped TiO_2 with exposed {001} facets on a graphene scaffold as photo-active hybrid nanostructures for reduction of carbon dioxide to methane

Wee-Jun Ong[1], Lling-Lling Tan[1], Siang-Piao Chai[1] (✉), Siek-Ting Yong[1], and Abdul Rahman Mohamed[2]

[1] *Low Carbon Economy (LCE) Group, Chemical Engineering Discipline, School of Engineering, Monash University, Jalan Lagoon Selatan, 46150 Bandar Sunway, Selangor, Malaysia*

[2] *Low Carbon Economy (LCE) Group, School of Chemical Engineering, Universiti Sains Malaysia, Engineering Campus, Seri Ampangan, 14300 Nibong Tebal, Pulau Pinang, Malaysia*

Received: 22 February 2014
Revised: 5 June 2014
Accepted: 12 June 2014

KEYWORDS

photocatalysis,
nitrogen-doped TiO_2,
{001} facet,
acid treated solvent exfoliated graphene,
carbon dioxide reduction,
visible light

ABSTRACT

Tailored synthesis of well-defined anatase TiO_2-based crystals with exposed {001} facets has stimulated incessant research interest worldwide due to their scientific and technological importance. Herein, anatase nitrogen-doped TiO_2 (N–TiO_2) nanoparticles with exposed {001} facets deposited on the graphene (GR) sheets (N–TiO_2-001/GR) were synthesized for the first time via a one-step solvothermal synthetic route using NH_4F as the morphology-controlling agent. The experimental results exemplified that GR was uniformly covered with anatase N–TiO_2 nanoparticles (10–17 nm), exposing the {001} facets. The percentage of exposed {001} facets in the N–TiO_2-001/GR nanocomposites was calculated to be ca. 35%. Also, a red shift in the absorption edge and a strong absorption in the visible light range were observed due to the formation of Ti–O–C bonds, resulting in the successful narrowing of the band gap from 3.23 to 2.9 eV. The photocatalytic activities of the as-prepared photocatalysts were evaluated for CO_2 reduction to produce CH_4 in the presence of water vapor under ambient temperature and atmospheric pressure using a low-power 15 W energy-saving daylight lamp as the visible light source—in contrast to the most commonly employed high-power xenon lamps—which rendered the process economically and practically feasible. Among all the studied photocatalysts, the N–TiO_2-001/GR nanocomposites exhibited the greatest CH_4 yield of 3.70 μmol·$g_{catalyst}^{-1}$, approximately 11-fold higher activity than the TiO_2-001. The enhancement of photocatalytic performance was ascribed to the effective charge anti-recombination of graphene, high absorption of visible light region and high catalytic activity of {001} facets relative to the {101} facets.

Address correspondence to chai.siang.piao@monash.edu

1 Introduction

Global warming, as a result of the emission of the anthropogenic greenhouse gases particularly carbon dioxide (CO_2), is attracting worldwide attention. Unfortunately, most of the thermochemical processes for CO_2 conversion require a huge amount of energy input, which results in the net increase of CO_2 emission. Therefore, for sustainable development, the advancement of converting CO_2 into energy-bearing products via a viable approach without further increasing the concentration of atmospheric CO_2 is an urgent task to address the ever-increasing challenges of climate change. Among the green and renewable energy projects that are underway, semiconductor photocatalysis has gained considerable interdisciplinary attention and much research fascination for their diverse potentials in energy and environmental applications. In this regard, photocatalytic reduction of CO_2 into useful hydrocarbons under visible light irradiation is a promising solution to circumvent both the energy and environmental crisis by recycling CO_2 to energy feedstock [1–3].

Since the first demonstration of photocatalytic water splitting using TiO_2 electrodes by Fujishima and Honda under ultraviolet (UV) light in 1972 [4], there has been significant progress in the design of efficient semiconductor photocatalysts. To date, the development of effective semiconductor-based photocatalysts for solving environmental problem and the remediation of energy shortages has become a hot research field. In this field, TiO_2 is by far the most researched photocatalytic material due to its long term stability, strong oxidizing power, high chemical inertness, corrosion resistant, non-toxicity, cost effectiveness and environmentally benign nature [5, 6]. Recently, the synthesis of crystals with highly reactive facets has sparked great research interest seeing that crystals usually exhibit fascinating surface-dependent properties [7, 8]. For anatase TiO_2, theoretical and experimental studies show that the {001} facets are the most reactive facets with a high surface energy. However, anatase TiO_2 crystals are usually dominated by the most naturally appearing and less reactive {101} facets which are thermodynamically more stable due to their lower surface energy than that of {001} facets [9]. The order of the average surface energies of anatase TiO_2 reported in the literature is 0.90 $J \cdot m^{-2}$ for {001} > 0.44 $J \cdot m^{-2}$ for {101} [10, 11]. During the crystal growth processes under equilibrium condition, the high energy {001} facets diminish rapidly and hence the crystal spontaneously transforms into a specific shape with exposed {101} facets (accounting for 94%) that minimize the total surface free energy [12]. This leads to a limited reactivity for anatase TiO_2. Therefore, the advancement of anatase TiO_2 with preferential high energy {001} facets has become an important approach for improving the photocatalytic applications. Since an important breakthrough in the synthesis of micro-sized anatase TiO_2 with ~47% exposed {001} facets by Yang et al. [7], extensive efforts have been focused on the preparation, characterizations, modifications and applications of anatase TiO_2 with {001} facets. However, the rapid recombination of photogenerated electron–hole pairs greatly limits the efficiency of the photocatalytic reaction. Hence, to inhibit the recombination of charge carriers and also extend the light absorption to the visible light region, a favorable conductive substrate is urgently demanded for the enhanced photocatalytic activity. The combination of TiO_2 with carbonaceous materials has attracted incessant research attention which can enhance the efficiency of photocatalytic activity [13].

In particular, graphene, known as a single atomic layer of graphite arranged in six-membered rings of carbon atoms, is a rising star on the horizon of materials science. The picturesque honey-comb-like and two-dimensional (2D) sp^2 hybridized graphene has become a hot spot on scientific research due to its extraordinary electrical, mechanical and thermal properties such as excellent mobility of charge carriers (250,000 $cm^2 \cdot V^{-1} \cdot s^{-1}$), large surface area (calculated value = 2,630 $m^2 \cdot g^{-1}$), high thermal conductivity (~5,000 $W \cdot m^{-1} \cdot K^{-1}$), optical transparency and good chemical stability [14–16]. Based on the unique properties of graphene, considerable efforts have been focused on the incorporation of graphene with TiO_2-based nanocomposites for a cornucopia of potential photocatalytic applications although it is still in its infancy [17, 18]. It is expected that the introduction of TiO_2-based nanocomposites with graphene will simultaneously result in superior electron transferability for lengthening the lifetime of

photoinduced charge carriers.

Up to now, different approaches have been developed to prepare individual or few layers of graphene sheets by exfoliating graphite flakes. The solution-phase isolation of graphene from graphite, which is the most common route, can be categorized in two different approaches. The first and most regularly used method is the modified Hummer's method using strong oxidizing agents to chemically exfoliate graphite to individual graphene oxide (GO) with abundance of oxygen moieties [19, 20]. However, it is widely known that exfoliated GO exemplifies poor electronic conductivity resulting from the interruption of the π-system by substitution with a significant amount of defects (oxygen functional groups) [21]. Therefore, various reducing agents such as $NaBH_4$ have been used to reduce GO for the restoration of sp^2 hybridized network [22]. The second approach employs the ultrasonic energy to directly exfoliate graphite in a suitable solvent such as *N*,*N*-dimethylformamide (DMF) to yield solvent exfoliated graphene (SEG) [23]. Without employing the use of strong oxidizing agents, we developed a facile, low-cost and efficient approach by performing acid pre-treatment for the first time to introduce minimal oxygen-containing groups on the SEG (referred to as acid treated SEG (ATSEG)) for a better interfacial contact with composites. It is anticipated that the electrical mobility of the ATSEG-based nanocomposites with a longer electronic mean free path was enhanced as compared to that of GO-based nanocomposites.

Herein, we demonstrate a facile and reproducible solvothermal route to engineer nano-sized nitrogen-doped TiO_2 with exposed {001} facets (N–TiO_2-001) dominant on the platform of SEG for the reduction of CO_2 to methane (CH_4) as energy feedstock. To the best of our knowledge, this is considered the first report on the use of ATSEG coupled with N–TiO_2-001 composite as a new class of visible-light-driven photocatalyst. Furthermore, our literature survey shows that no one has ever reported the use of {001}-faceted TiO_2-based photocatalysts for the photocatalytic conversion of CO_2 under a UV or visible light source thus far. Therefore, another significance of our work is that the newly developed photocatalysts are applied to convert CO_2 to CH_4 using water as the sacrificial agent and low-power 15 W energy-saving daylight lamp as the visible light source in a custom-fabricated reactor system under ambient conditions, in contrast to the most commonly employed high-power halogen and xenon lamps. This renders the entire process practically feasible and economically viable.

2 Experimental

2.1 Materials

Graphite powder (average particle size of 45 μm), DMF (99.8%), titanium(IV) butoxide (TBOT) (97%), ethylene glycol (EG) (99%), acetic acid (HAc) (99.7%), 2-propanol anhydrous (99.5%), diethylenetriamine (DETA) (99%) and ammonium fluoride (NH_4F) (98.0%) were supplied by Sigma Aldrich. Sulphuric acid (95%–97%), nitric acid (70%) and ethanol (96%) were supplied by Chemolab. All chemicals were reagent-grade and used as received without any further purification.

2.2 Synthesis of ATSEG

ATSEG was synthesized from graphite powder by an exfoliation method in an organic solvent followed by acid pre-treatment. Typically, 1 g of graphite powder was placed into 100 mL of DMF and sufficiently subjected to ultrasonication in an ultrasonic water bath for 3 h at 40 kHz and 180 W. The resultant dispersion was then centrifuged for 15 min at 8,000 rpm. Afterwards, the SEG was filtered and washed with ethanol to remove the excess DMF. Finally, the obtained solid was pre-treated with acid to introduce oxygen-containing functional groups on the ATSEG surface to ease the coupling of TiO_2 in the later stage. Acid pre-treatment was conducted by continuously stirring SEG in a mixture of nitric acid and sulphuric acid mixed at a volume ratio of 1:3 at the concentration of 5 M each under reflux at 100 ˚C for 4 h. The mixture was then filtered and repeatedly washed with deionized water until neutral pH to remove the acid remnant. The ATSEG was collected and dried at 70 ˚C in an oven overnight prior to the storage in the powder form for further use.

2.3 Synthesis of TiO_2-based/GR hybrid nanocomposites

The synthesis of N–TiO_2 nanoparticles with exposed {001} facets on graphere sheets (N–TiO_2-001/GR) nanocomposites was performed as follows. In a typical synthesis route, 0.18 g ATSEG was dispersed in 33 mL of EG and 17 mL of deionized (DI) water with ultrasonication for 1 h at 40 kHz and 180 W to form a homogeneous solution consisting of exfoliated ATSEG. 0.88 g NH_4F was dissolved in 4 mL of DI water and added into the ATSEG solution under vigorous stirring. On the other hand, 10 mL of 2-propanol was mixed with 0.06 mL of DETA to form part A. Next, 2 mL of TBOT was introduced into a mixture of 7.3 mL of EG and 1.2 mL of HAc to form part B. Subsequently, part A and part B were mixed thoroughly to obtain part C. The solution from part C was added dropwise into the ATSEG suspension immersed in an ice bath under vigorous stirring. The molar ratio of Ti to F was fixed at 1:4. The resultant mixture was then stirred for another 30 min to achieve a uniform precursor solution. Successively, the mixed suspension was transferred into a 120 mL of Teflon-lined stainless steel autoclave and sealed tightly. The autoclave was heated to 190 ℃ and kept there for 10 h. After solvothermal treatment, the reaction system was cooled naturally to room temperature. The nanocomposite, denoted as N–TiO_2-001/GR, was centrifuged, filtered and washed thoroughly with ethanol for three times. Finally, the product was fully dried in an oven at 70 ℃ overnight and then milled into an ultrafine powder. The initial mass ratio of ATSEG to TBOT was calculated to be 0.20.

For comparison, the starting material without adding NH_4F (denoted as N–TiO_2/GR) was synthesized using a similar solvothermal route. Meanwhile, the starting material without adding NH_4F, 2-propanol and DETA (denoted as TiO_2/GR) was produced in the same solvothermal conditions. TiO_2-001/GR was formed using the same solvothermal conditions without adding 2-propanol and DETA. N–TiO_2-001 nanocomposites were prepared in the absence of ATSEG suspension via the above solvothermal method. Lastly, pure TiO_2-001 was obtained by a similar procedure in the absence of ATSEG suspension, 2-propanol and DETA solutions.

2.4 Characterization

The surface morphology and elemental composition of the developed photocatalysts were analyzed by field emission scanning electron microscopy (FESEM) and energy-dispersive X-ray (EDX) (Hitachi SU8010). The specimens for FESEM analysis were prepared by depositing a drop of diluted suspensions in ethanol on a silicon wafer. Scanning transmission electron microscopy (STEM) images were taken on a FESEM at an accelerating voltage of 30 kV. The particle size distribution of the samples was conducted by measuring the size of the nanoparticles using the Image J software. High resolution transmission electron microscopy (HRTEM) images were taken with a JEOL JEM-2100F microscope operated at 200 kV. The TEM sample was created by depositing a drop of diluted suspensions in ethanol on a lacey-film-coated copper grid. Powder X-ray diffraction (XRD) patterns were obtained over the diffraction angle range (2θ) 0–90° on a Bruker D8 Discover X-ray diffractometer using Ni-filtered Cu-Kα radiation (λ = 0.154056 nm) as the X-ray source at a scan rate of 0.02 °·s^{-1} operated at 40 kV and 40 mA. Raman spectra were recorded at room temperature using Renishaw inVia Raman Microscope in the back-scattering geometry with Ar^+ laser excitation at 514 nm in the range of 100–2,000 cm^{-1}. X-ray photoelectron spectroscopy (XPS) measurements were performed using AXIS Ultra DLD, Kratos, equipped with a monochromated Al Kα X-ray source (1,486.6 eV) at a pressure of 7.6×10^{-9} torr and a pass energy of 20 eV. All the binding energies were referenced to the C 1s peak at 284.6 eV of the surface carbon. Peak deconvolution and quantification of elements were accomplished using OriginPro 8.5. Fourier transform infrared (FTIR) spectroscopy was performed using a Thermo-Nicolet iS10 FTIR spectrometer in the range of 400–4,000 cm^{-1} with 0.1 cm^{-1} resolution. The sample was mixed with KBr, pressed into self-supported pellets and measured in the transmission mode. Ultraviolet–visible (UV–Vis) absorbance spectra were determined using a UV–Vis spectrophotometer (Agilent, Cary 100) equipped with an integrated sphere. The absorbance spectra of the samples were analyzed at ambient temperature in the wavelength range of 200–800 nm. The band gap

energies of the photocatalysts were determined from the Kubelka–Munk (KM) function, F(*R*) where *R* is the reflection coefficient of the sample and the extrapolation of Tauc plot to the abscissa of photon energy. The surface area of the prepared samples was measured by multipoint Brunauer–Emmett–Teller (BET) of N_2 adsorption/desorption at –196 ℃ using a Micrometrics ASAP 2020. Prior to the adsorption measurement, all samples were degassed at 180 ℃ for 4 h to remove any water and other contaminants. Thermogravimetric analysis (TGA) was performed using TA Instruments Thermogravimetric Analyzer Q50 at a heating rate of 10 ℃·min^{-1} from room temperature to 900 ℃ under purified air flow. The photoluminescence (PL) emission spectra were measured at room temperature by 325 nm He–Cd laser as an excitation light source using Renishaw inVia Raman Microscope. The emission spectra were scanned from 400 to 750 nm.

2.5 Evaluation of photocatalytic activity

Photocatalytic activity of the developed TiO_2-based/GR nanocomposites was performed in a CO_2 photoreduction system at ambient temperature (25 ± 5 ℃) and atmospheric pressure (1 bar) in a continuous gas flow reactor as reported in our previous work [13]. The CO_2 photoreduction process was conducted under visible light irradiation with a maximum light emission intensity of 15 W using an energy-saving daylight lamp (Philips, TORNADO 15 W WW E27 220–240 V 1CT) to provide a full spectrum emission without any filter to simulate the sunlight source for a total of 10 h. The developed photocatalysts were coated onto glass rods and then loaded into quartz tubes, which were then placed under the visible light for irradiation. The coating of photocatalysts on the glass rods was carried out by preparing thick slurry comprising 1 g of powder samples and 1.5 mL of ethanol. The coating was done using a dip-coating method. Subsequently, the coated layer of the photocatalysts on the glass rods was obtained by drying in an oven at 140 ℃ for 4 h to improve the adhesion. Upon loading of glass rods coated with the photocatalysts, high purity of CO_2 (99.99%) was flowed through a water bubbler to produce a mixture of CO_2 and water vapour, which acted as a sacrificial reagent, at atmospheric pressure. Before the irradiation of visible light, wet CO_2 at a flow rate of 30 mL·min^{-1} was first flowed through the quartz tube reactor loaded with coated glass rods for 1 h to ensure that the air in the reactor system was totally eliminated and also to achieve complete adsorption of gas molecules. After 1 h of purging, the light was turned on and CO_2 photoreduction process was conducted with a controlled flow rate of CO_2 at 5 mL·min^{-1} using a mass flow controller. The temperature in the reactor was closely monitored with a thermocouple attached to a digital temperature reader. The average intensity of the light was measured to be 8.5 mW·cm^{-2} by utilizing a pyranometer (Kipp and Zonen type CMP 6). The light spectrum of the visible light was recorded using an Avantes fiber optic spectrometer (AvaSpec-128) equipped with a cosine collector and it was in the range of 400–625 nm (Fig. S1 in the Electronic Supplementary Material (ESM)), with the distance between the light source and the photoreactor being 5 cm. During the CO_2 photoreduction process, the product gas was collected in a gas bag and its composition was analyzed by a gas chromatography (GC) (Agilent 7890A) equipped with both thermal conductivity detector (TCD) and flame ionized detector (FID). The entire photoreaction system was enclosed in a black box to avoid any interference of light source from the surrounding. The photocatalytic experiments were performed in duplicate under similar reaction conditions to ensure the reproducibility of the catalytic activity in which consistent results with significant small variations were obtained. The total yield of CH_4 produced was calculated based on Eq. (1)

$$\text{Total } CH_4 \text{ yield} = \frac{\text{Total amount of } CH_4 \text{ produced (μmol)}}{\text{Amount of photocatalyst used } (g_{catalyst})} \quad (1)$$

3 Results and discussion

3.1 Synthesis approach

In this work, N–TiO_2-001/GR were fabricated by self-assembly employing an NH_4F-mediated self-growing method instead of the conventional HF strategy. As

the ATSEG contains oxygen functional groups such as hydroxyl (–OH) and carboxyl (–COOH), TBOT can be grafted on the ATSEG surfaces via chemisorption at the molecular level. Ultrasonication assisted the dispersion of ATSEG in the solution and promoted the reaction of TBOT with the functional groups on the ATSEG surfaces. It should be noted that TBOT is very sensitive to H_2O, and even the moisture in the air can easily cause the decomposition of TBOT [24]. This resulted in the formation of large particle size and inhibited the homogeneous growth of TiO_2 on the ATSEG in the reaction medium. To overcome the agglomeration of TiO_2, we introduced two reagents namely EG and HAc to co-control the hydrolysis rate of TBOT. In addition, the mixtures were also pre-chilled in an ice bath to further reduce the hydrolysis rate. The whole solvothermal protocol is schematically shown in Fig. 1.

3.2 Morphology and phase structure

The morphology of the ATSEG and a series of TiO_2-based/GR nanocomposites was characterized by FESEM and HRTEM. Upon sonication for 3 h and acid pre-treatment for 4 h, the ATSEG revealed a 2D flexible, transparent and wrinkled paper-like structure composed of crumpled few (3–6) layers thick graphene sheets (Fig. 2 and Figs. S2(a)–S2(d) in the ESM).

After solvothermal synthesis at 190 ˚C for 10 h with the addition of EG and HAc into the reaction system, graphene sheets, which possessed lateral dimensions of 1–10 microns, were homogeneously decorated with N–TiO_2-001 nanoparticles as presented in Figs. 3 and 4 and Figs. S6(a) and S6(b) (in the ESM). Figure 3(b) depicts an enlarged image of part of Fig. 3(a) where it can be seen that after the end of solvothermal treatment, the N–TiO_2-001 exhibited a narrow size distribution ranging from 10 to 17 nm with an average size of 13.2 nm (Fig. 3(c)) and uniformly covered the ATSEG surface with minimum agglomeration relative to the {001}-faceted N–TiO_2 nanoparticles (Figs. S4(c) and S4(d) in the ESM). The fringes of graphene could be explicitly identified, which is convincing evidence of the presence of graphene sheets under the N–TiO_2-001 layer. Surprisingly, we found that even after 15 min of sonication during the preparation of the FESEM specimen, the N–TiO_2-001 nanoparticles

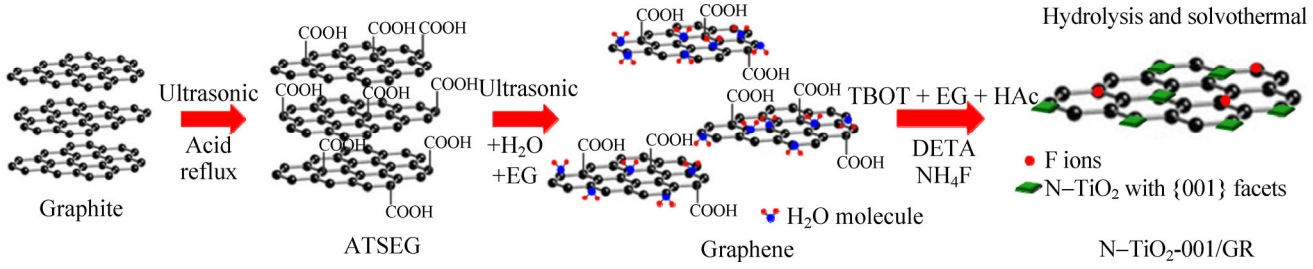

Figure 1 Schematic illustration for the development of N–TiO_2-001/GR via a one-step solvothermal treatment by employing TBOT as the titanium precursor, DETA as the nitrogen source and NH_4F as the morphology controlling agent.

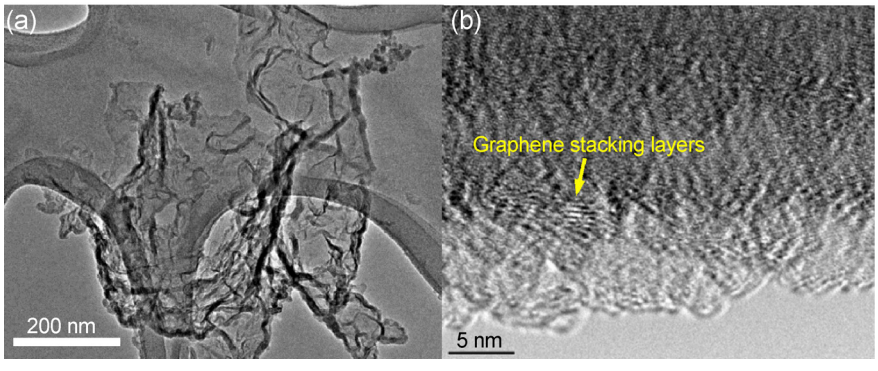

Figure 2 (a) TEM image of ATSEG. (b) HRTEM image of the thin edge of ATSEG, revealing 3–6 layers of graphene.

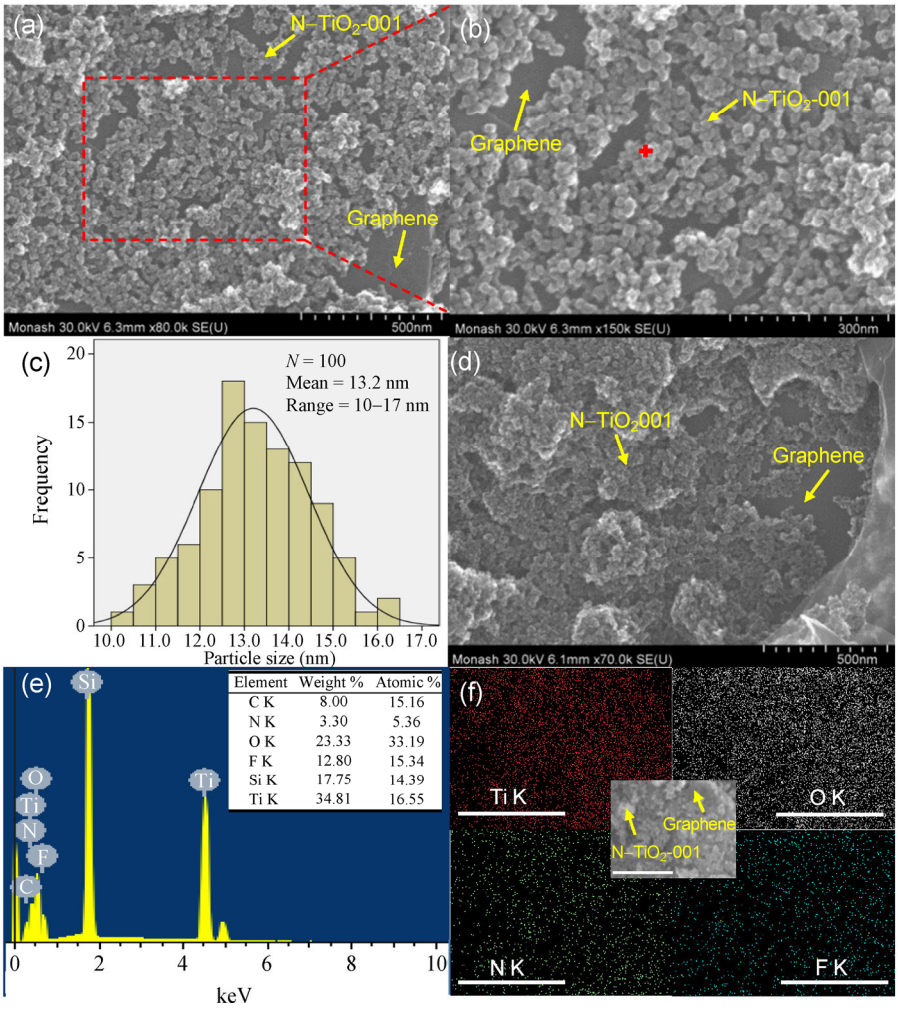

Figure 3 (a) Low magnification and (b) high magnification images of N–TiO_2-001/GR. (c) Particle size distribution of N–TiO_2 nanocrystals with exposed {001} facets supported on ATSEG surface. (d) FESEM image of N–TiO_2-001/GR after 15 min of sonication for the preparation of FESEM specimen. (e) EDX spectrum of N–TiO_2-001/GR at the position "+" from the image shown in panel (b). (f) EDX mapping of Ti (red), O (white), N (green) and F (blue) elements, respectively of the N–TiO_2-001/GR sample (scale bar: 1 μm). The inset of (f) is the corresponding FESEM image of N–TiO_2-001/GR used for elemental mapping (scale bar: 1 μm).

were still strongly adhered to the surface of ATSEG sheets (Fig. 3(d)), showing that there was a strong interaction between the N–TiO_2-001 nanoparticles and the ATSEG sheets, which is of utmost significance for effective electron transfer kinetics. The Ti–O–C bond is believed to ensure a compact connection between N–TiO_2-001 and ATSEG. It is proposed that the strong chemical bonding between N–TiO_2-001 nanoparticles and ATSEG sheets can be ascribed to the polar interactions which promote interfacial charge carrier transfer in the hybrid heterostructures.

The compositions and element mapping over the desired region of the N–TiO_2-001/GR nanocomposites were investigated with EDX as shown in Figs. 3(e) and 3(f). Ti, O, C, N, F and Si were detected in the nanocomposites. The Si peak was from the substrate (silicon wafer). The presence of N, Ti and O atoms corroborated the development of N–TiO_2-001. The F species detected can be ascribed to the typical surface Ti–F bonds, which could substantially reduce the surface energy and thus enhance the stability of {001} facets [7]. The presence of a C peak could be related to ATSEG, even if some interference resulted from the use of carbon tape to fix the silicon wafer for the FESEM analysis. Elemental mapping of Ti, O, N and F was also taken to further confirm the distribution of N–TiO_2-001 on the ATSEG (Fig. 3(f)). It can be seen that N element was evenly distributed on the TiO_2.

On the other hand, obvious agglomeration of N–TiO_2-001 was observed (Fig. S7 in the ESM) in the absence of EG and HAc in the synthesis mixture, highlighting the importance of both reagents in lowering the hydrolysis rate of TBOT. For comparison, it was noted that N–TiO_2 nanoparticles without well-defined {001} facets were synthesized when NH_4F was not used as the capping agent (Fig. 5 and Figs. S6(c) and S6(d) in the ESM), implying that NH_4F played a crucial role in stabilizing the high surface energy of {001} facets. The obtained particle size was much smaller than that of {001}-faceted N–TiO_2 nanoparticles, being in the range of 5–10 nm with a mean value of 7.0 nm (Fig. 5(d)), showing that the stabilization of top and bottom {001} facets by fluoride ions makes the overall crystal size larger. No obvious agglomeration of particles could be seen, confirming the key role of graphene as a scaffold to anchor N–TiO_2 particles and improve the interaction between the semiconductor and graphene. In the absence of ATSEG, poorer dispersion and larger particle size (mean value of 19.7 nm) of the N–TiO_2-001 were observed (Figs. S4(c) and S4(d) in the ESM), implying ATSEG had a great influence on the crystal growth of N–TiO_2-001. Hence, this confirms the role of ATSEG as a support material for the *in situ* growth and suppression of the aggregation of N–TiO_2-001.

It can be inferred from the FESEM results that close interfacial contact between N–TiO_2-001 and graphene was attained in the as-synthesized N–TiO_2-001/GR nanocomposites, and a deeper insight into the detailed structures of the products was obtained using HRTEM analysis. As can be seen from Figs. 4(a) and 4(b), the as-prepared N–TiO_2-001 nanocrystals were adequately dispersed on the ATSEG sheets, which is in consonance with the FESEM images (Figs. 3(a) and 3(b)). The structure consisted of well-faceted and well-defined nanocrystals with a uniform particle size of 10–17 nm. Viewed from different directions, the square and truncated rhombus shape could be observed (Fig. 4(b)), which can be attributed to a highly truncated octahedral bipyramidal structure with the NH_4F as a shape-directing agent. The HRTEM image (Fig. 4(c)) revealed that the lattice spacing parallel to the top

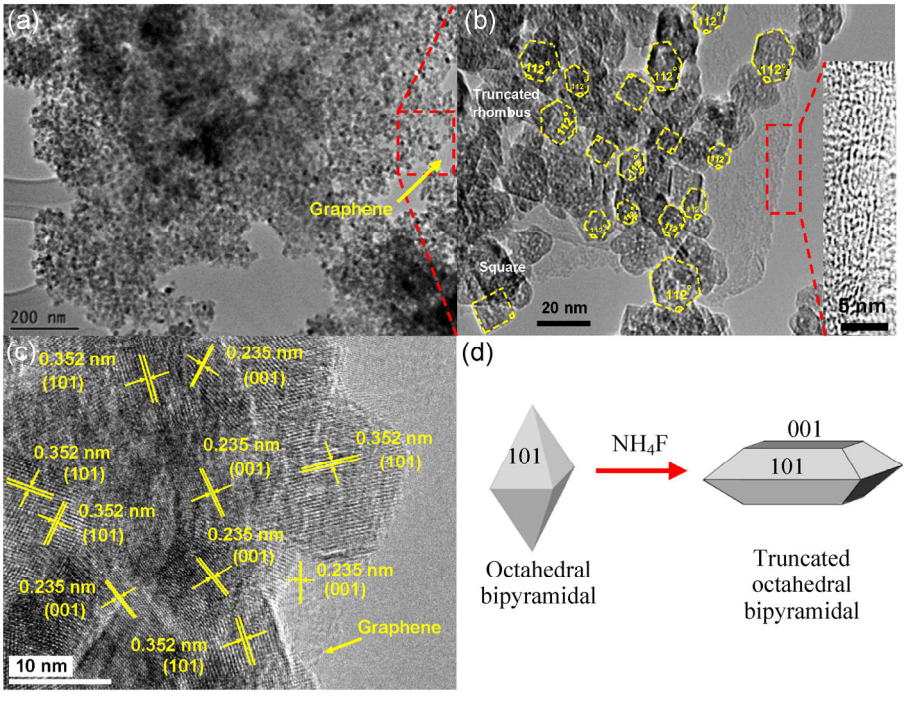

Figure 4 (a) TEM image of N–TiO_2-001/GR, showing the thin ATSEG sheet and dispersion of highly reactive {001} facets of N–TiO_2. (b) Part of the enlarged TEM image of N–TiO_2-001/GR corresponding to the red rectangle from the image shown in panel (a) (inset is the HRTEM image of the thin edge of ATSEG, revealing 4–6 layers of graphene). (c) HRTEM image of N–TiO_2-001/GR. (d) Morphology evolution of N–TiO_2-001 crystals using NH_4F as the shape-directing agent to stabilize the high energy {001} facets.

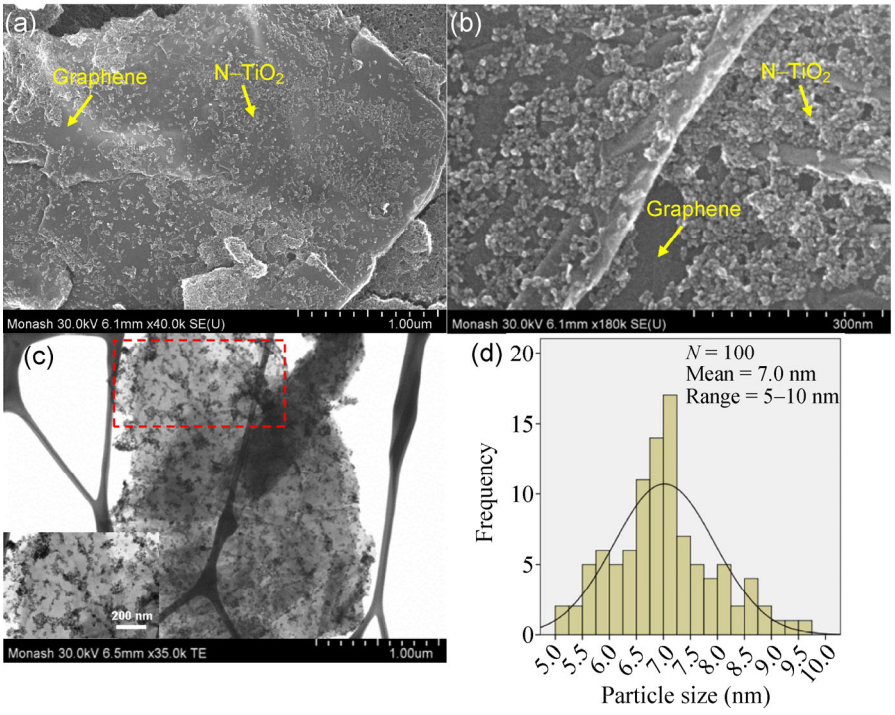

Figure 5 Electron microscopy of the N–TiO_2/GR nanocomposites without exposed highly reactive {001} facets (no addition of NH_4F as the morphology controlling agent): (a) Low magnification FESEM image, (b) high magnification FESEM and (c) STEM image (inset is the enlarged STEM image corresponding to the red rectangle from the image shown in panel (c)). (d) Particle size distribution of N–TiO_2 nanocrystals without exposed {001} facets supported on the ATSEG surface.

and bottom facets was 0.235 nm, corresponding to the (001) planes of anatase TiO_2, which indicates the top and bottom facets are the (001) and (00$\bar{1}$) planes, respectively [25]. Additionally, clear atomic planes with a lattice spacing of 0.352 nm were also clearly observed, which correspond to the (101) planes of anatase TiO_2. From the symmetry of N–TiO_2-001 single crystal, combined with the morphologies in the TEM images, the two flat and square surfaces and eight isosceles trapezoidal surfaces in the crystal structure were assigned to {001} and {101} facets respectively (Fig. 4(d)). Also, an angle of ca. 112°, consistent with the interfacial angle between {001} and {101} facets, was observed in the hexagonal-shaped particles [26] (Fig. 4(b)), implying that the particle showed flat surfaces of {001} and {101} facets. From the size and geometry, the percentage of exposed highly reactive {001} facets in the nanocomposite was calculated by the method described by Yu et al. [27]. On the basis of the TEM results using a total of fifty N–TiO_2-001 nanocrystals, the average percentage of {001} facets was estimated to be ca. 35% (see Fig. S3 in the ESM for detailed calculations). According to the theory estimation and experimental results, the percentage of exposed {001} facets for the TiO_2 nanoparticles was less than 10% (ca. 6%) [28]. This confirms that the fluoride ions from NH_4F played a prominent role in the formation of TiO_2 with reactive {001} facets.

Figure 6 clearly shows that all diffraction peaks of N–TiO_2-001/GR match well with the crystal structure of the anatase TiO_2 (Fig. 6(a)). The peaks at 2θ values of 25.3°, 37.8°, 48.0°, 53.9°, 55.0°, 62.7°, 75.0° can be

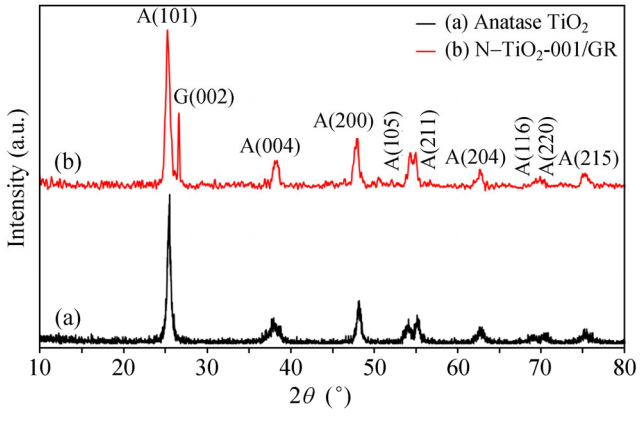

Figure 6 XRD patterns of (a) pure anatase TiO_2 and (b) N–TiO_2-001/GR (A denotes anatase and G denotes graphene).

well-indexed to (101), (004), (200), (105), (211), (204) and (215) crystal planes of anatase TiO_2 crystallites respectively (space group, $I4_1/amd$; JCPDS no. 21–1272) [29]. Additionally, the peak at 2θ value of 26.5° represented the presence of graphene in the nanocomposites [30]. No rutile phase was detected due to the low reaction temperature employed in this work. By applying the Debye–Scherrer formula, the crystallite size of the anatase TiO_2 in the nanocomposites was 13.6 nm based on the most intense peak (101), which conformed well to the FESEM and HRTEM results. The (101) and (200) diffraction peaks were chosen to determine the anatase lattice parameters of the doped TiO_2 using Eq. (2) [31]

$$d^{-2}_{(hkl)} = h^2a^{-2} + k^2b^{-2} + l^2c^{-2} \quad (2)$$

where a, b and c are the lattice parameters ($a = b \neq c$ for anatase), hkl is the crystal plane index and $d_{(hkl)}$ is the crystal plane distance of (hkl). The calculated cell parameters of the N–TiO_2/GR (a = 3.7845 Å, c = 9.5143 Å) and N–TiO_2-001/GR (a = 3.7852 Å, c = 9.5139 Å) nanocomposites are slightly different as compared to the cell parameters of pure anatase TiO_2/GR (a = 3.7770 Å, c = 9.5010 Å), confirming the successful doping of nitrogen into the lattice of TiO_2. A similar phenomenon has been observed for the incorporation of carbon dopants into the TiO_2 lattice [27].

3.3 Raman spectra

Figure 7(a) shows a comparison of the Raman spectra of graphite, ATSEG and N–TiO_2-001/GR nanocomposites. In the case of graphite and ATSEG, there were two distinct Raman signals, i.e. a D band and a G band at ca. 1,342 and 1,578 cm^{-1} respectively (Figs. 7(b1) and 7(b2)). Of particular interest is the intensity ratio of the D and G bands, I_D/I_G, which is a measure of the relative concentration of local defects or disorder (particularly the sp^3 hybridized defects) relative to the sp^2 hybridized graphene domains [17]. As could be clearly observed, the I_D/I_G ratio of ATSEG was 0.23, which was higher than 0.17 for graphite. This indicates that acid pre-treatment had effectively introduced defects (oxygen-containing functional groups) on the graphene sheets, which can potentially be utilized as a platform for the coupling of N–TiO_2 via electronic interactions. The effective decoration of N–TiO_2 on the ATSEG was evidenced by the FESEM images in Fig. 3. In particular, the photograph in Fig. 7(c) shows that, unlike graphite flaked, ATSEG could disperse well in water for more than 12 h without obvious sedimentation, suggesting high dispersing stability which enables the formation of exfoliated ATSEG in water.

In addition, the four peaks observed in the low frequency region were assigned to the $E_{g(1)}$ (149 cm^{-1}), $B_{1g(1)}$ (399 cm^{-1}), $A_{1g} + B_{1g(2)}$ (516 cm^{-1}) and $E_{g(2)}$ (637 cm^{-1}) modes of pure anatase TiO_2 in the N–TiO_2-001/GR nanocomposites (Fig. 7(a4)), which matched well with the spectrum of anatase N–TiO_2-001 (Fig. 7(a3)). The peak shift of the Raman spectra was analyzed using the most intense peak at ca. 149 cm^{-1} ($E_{g(1)}$). Generally, the peak shift is mainly affected by the size of nanomaterial as well as defects and temperature [32]. However, in this investigation, the same laser source was used for recording all Raman spectra. Thus, local heating and various excitation power outputs from the laser could be ruled out as a source of any shifts. As a result, the blue shift of the $E_{g(1)}$ peak can be ascribed to the surface pressure and phonon confinement effects due to the decrease of particle size of N–TiO_2-001 formed on the ATSEG sheets and also the strain developed on the N–TiO_2-001/GR surface. This provides clear evidence of a strong chemical interaction between N–TiO_2-001 and ATSEG sheets in the nanocomposite, which is pivotal for providing effective electron transfer channels. The observed spectrum variation was in agreement with the previously reported data by Perera et al. [21].

On the other hand, the G band shifted from 1,578 to 1,582 cm^{-1} while the D band moved from 1,342 to 1,335 cm^{-1} in the N–TiO_2-001/GR nanocomposites (Fig. 7(b)). These shifts in the Raman peaks could also be attributed to the chemical interaction between N–TiO_2-001 and ATSEG. Similar findings have been reported by Lu et al. [33] and Gu et al. [34]. After the solvothermal reaction, the I_D/I_G ratio of N–TiO_2-001/GR was reduced from 0.23 to 0.19, which could be due to the removal of carboxyl groups and the restoration of sp^2 hybridized carbon (increased graphitization) resulting from the solvothermal reduction process,

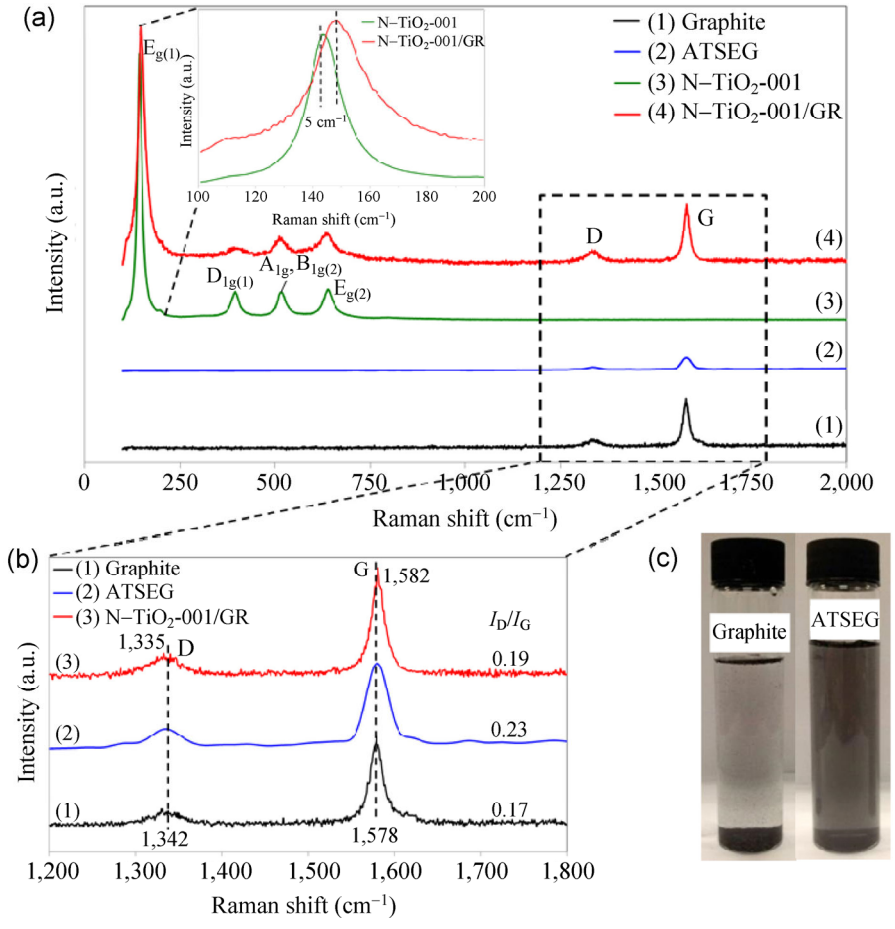

Figure 7 (a) Raman spectra of (1) graphite flake, (2) ATSEG, (3) N–TiO_2-001 and (4) N–TiO_2-001/GR (inset is the blue shift of $E_{g(1)}$ bands of the N–TiO_2-001/GR compared to N–TiO_2-001). (b) Characteristic D and G bands of (1) graphite flake, (2) ATSEG and (3) N–TiO_2-001/GR along with the I_D/I_G ratio. (c) Digital photograph of graphite and ATSEG dispersions in deionized water at a concentration of 0.2 mg·mL^{-1}.

and thus indicating a better repair mechanism [21, 35, 36]. Thus, the decreasing I_D/I_G ratio in the nanocomposites suggested that the solvothermal method we employed led to more graphene content without decreasing the average size of the sp^2 domain and retaining the large sp^2 domains.

3.4 XPS analysis

The successful functionalization of graphene sheets and N–TiO_2-001 in N–TiO_2-001/GR was confirmed by XPS. The peaks of titanium, oxygen, nitrogen, fluorine and carbon could be detected in the survey spectrum of N–TiO_2-001/GR (Fig. 8(a)). There were two distinct peaks at binding energies of 459.9 and 465.7 eV for the Ti 2p XPS spectrum (Fig. 8(b)). These can be attributed to the Ti $2p_{3/2}$ and Ti $2p_{1/2}$ spin-orbital split photoelectrons in the Ti^{4+} chemical state, respectively [37]. The splitting value of 5.8 eV between these bands is characteristic of the Ti^{4+} species in anatase TiO_2 [38]. A peak for F 1s at 685.4 eV was observed, which is a typical value for Ti–F bonds due to the surface fluorination of TiO_2 by NH_4F [35]. Moreover, the peak at ca. 400 eV can be ascribed to the incorporated nitrogen dopant in TiO_2 as interstitial N or Ti–O–N (Fig. S10 in the ESM), which agrees well with the literature [39, 40]. The amount of N dopant was ca. 5.01 atom% based on the XPS analysis. In addition, the main C 1s peak located at 285.2 eV was assigned to the C–C, C=C and C–H bonds (sp^2) of graphene (Fig. 8(c)) [29]. No C 1s peak at 281 eV, characteristic of Ti–C bonds, was detected, suggesting that carbon was not doped into the N–TiO_2-001 lattice [41, 42]. The peaks at binding energies of 286.5–287.0 and 288.0–288.5 eV can be attributed to C–O and

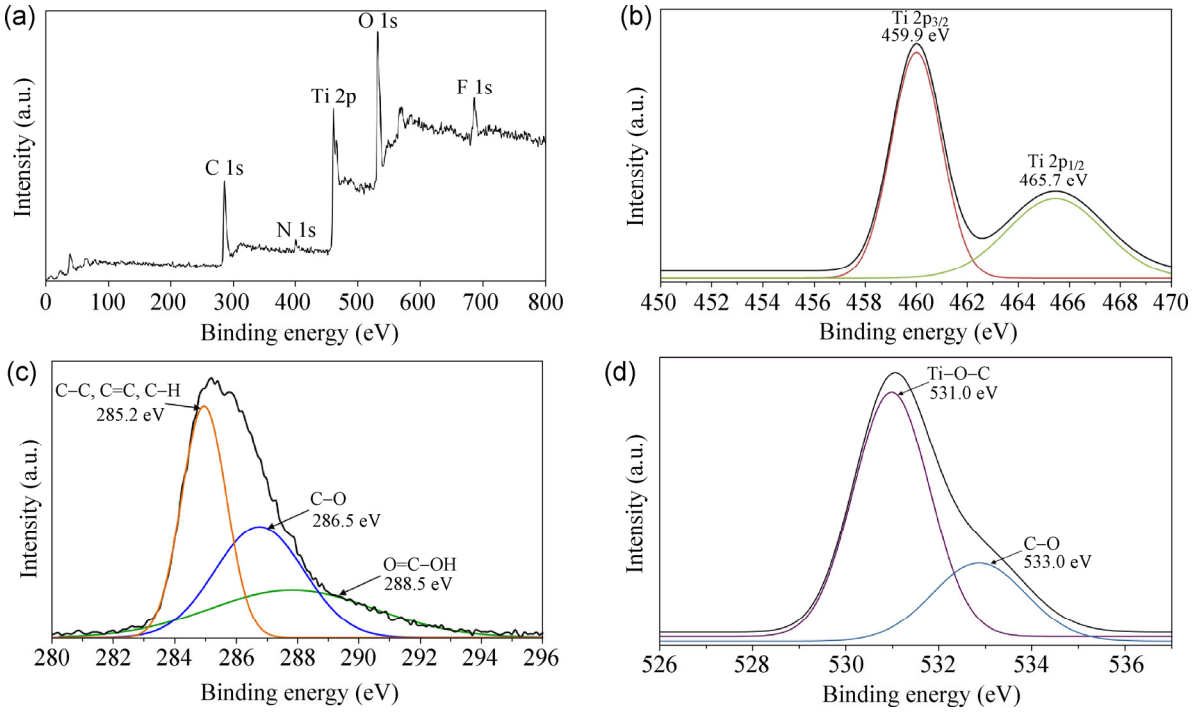

Figure 8 (a) Full XPS spectrum of N–TiO_2-001/GR nanocomposites. High resolution XPS spectra of (b) Ti 2p, (c) C 1s and (d) O 1s for N–TiO_2-001/GR nanocomposites.

O=C–OH oxygen-containing carbonaceous bands, respectively [37, 43]. The presence of such a surface functional group suggests that the –OH groups on the TiO_2 could react with the –COOH groups on the ATSEG surface via esterification to form O=C–O–Ti bonds. This can be further evidenced by the O 1s XPS spectrum (Fig. 8(d)), whereby the dominant peak at 531.0 eV can be well-indexed to O in Ti–O–C bonds [35]. Confirmatory evidence using FTIR could be attained for the formation of Ti–O–C bonds (Fig. S14 in the ESM), consistent with the reported literature [33, 44]. All these results further confirmed the doping of interstitial N- into the TiO_2 lattice, the successful integration between N–TiO_2-001 and graphene, and the strong interaction among Ti, O and C atoms after the solvothermal treatment.

3.5 UV–Vis diffuse reflectance spectra

Figure 9 shows the UV–Vis diffuse reflectance spectra of TiO_2-001, N–TiO_2-001, TiO_2-001/GR and N–TiO_2-001/GR. The pure TiO_2-001 sample displayed an intense transition in the UV region mediated by the intrinsic band gap absorption of TiO_2, resulting from the electron transitions from the valence band (VB) to conduction band (CB) (O 2p → Ti 3d) [40]. The introduction of nitrogen into the crystalline lattice of TiO_2 (N–TiO_2-001) modified the electronic band structure of TiO_2 leading to the formation of N-dopant levels above the O 2p VB, resulting in the absorption of visible light. Evidently, an additional visible light absorption shoulder between 400 and 550 nm was formed in the yellow N–TiO_2-001 nanocomposites in contrast to the undoped TiO_2-001, showing that N atoms were successfully doped into the TiO_2-001 lattice. More importantly, although the {001} facets of N–TiO_2-001 were stabilized by the presence of fluoride ions, it is known that the doping of fluoride cannot introduce visible light absorption; this has been widely reported in other studies [45]. This suggests that the visible light absorption was directly from the localized states of N 2p above the VB. Further incorporation of graphene caused a red shift in the absorption edge implying that carbon was incorporated with TiO_2-001 and N–TiO_2-001, and the layered graphene acted as a support for immobilization of both TiO_2-001 and N–TiO_2-001.

The broad background absorption of both TiO_2-001/GR and N–TiO_2-001/GR nanocomposites was

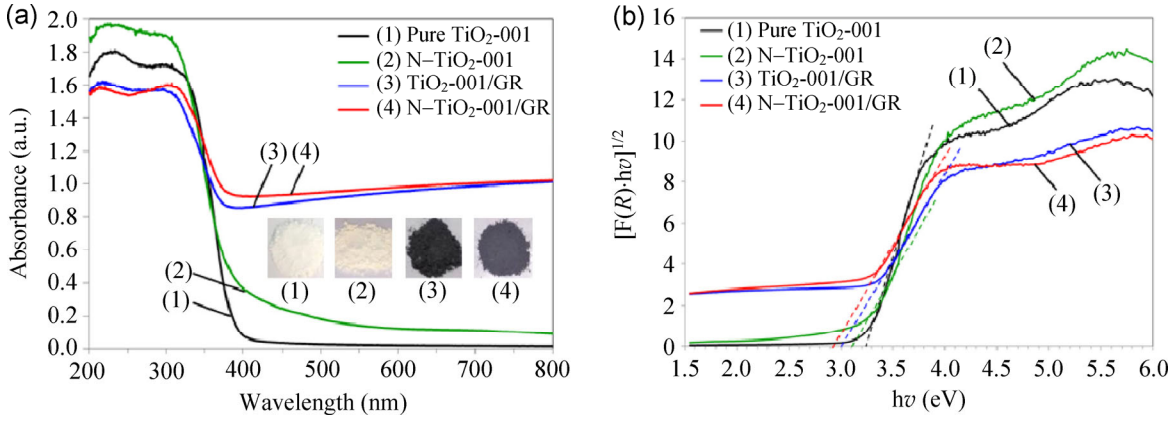

Figure 9 (a) UV–Vis diffuse reflectance absorption spectra of pure TiO_2-001, N–TiO_2-001, TiO_2-001/GR and N–TiO_2-001/GR nanocomposites (inset shows the colors of photocatalysts: (1) pure TiO_2-001, (2) N–TiO_2-001, (3) TiO_2-001/GR and (4) N–TiO_2-001/GR). (b) The plot of transformed KM function vs. energy of light for pure TiO_2-001, N–TiO_2-001, TiO_2-001/GR and N–TiO_2-001/GR nanocomposites.

extended into the visible light region, which can be attributed to the presence of graphene. On top of that, both nanocomposites displayed broad background absorption in the visible light range in the presence of graphene, which was supported by the color change from white to grey (inset of Fig. 9(a)). A Tauc plot obtained via the transformation based on the modified KM function vs. the energy of the light absorbed is shown in Fig. 9(b). The estimated band gap energies of the pure TiO_2-001, N–TiO_2-001, TiO_2-001/GR and N–TiO_2-001/GR nanocomposites were extrapolated to be 3.23, 3.10, 3.0 and 2.9 eV respectively. It is noted that the band gap of N–TiO_2-001 is smaller than that of TiO_2-001, signifying that there were some localized 2p states due to the N dopants being introduced in the band gap of TiO_2 [46, 47].

Furthermore, the successful narrowing of the band gap of both TiO_2-001/GR and N–TiO_2-001/GR nanocomposites can be attributed to the introduction of graphene into the matrix of the nanocomposites increasing effective visible light utilization. It is believed that the formation of Ti–O–C bonds (as shown by the XPS analysis) between graphene and TiO_2 in both TiO_2-001/GR and N–TiO_2-001/GR nanocomposites led to a reduction in band gap to 3.0 and 2.9 eV respectively. This has also been observed for other GR-based semiconductor photocatalysts and can be assigned to the chemical bonding between the semiconductor and graphene support [48]. A further reduction in band gap to 2.9 eV was observed in the N–TiO_2-001/GR nanocomposites, which was attributed to the presence of abundant localized states of N 2p above the O 2p VB as a result of incorporation of N dopants into the TiO_2 lattice [49, 50]. In addition to graphene, an extended optical absorption has also been observed in our previous work on semiconductor-carbon nanotubes (CNTs) photocatalysts, which could be due to the electronic interactions between TiO_2 and carbon [13]. Therefore, the synergic contributions from both the ATSEG and N-doping result in visible light absorption over a wide range of wavelengths, with reduced band gap energy. The UV–Vis spectra for TiO_2/GR and N–TiO_2/GR are provided in Fig. S12 (in the ESM).

3.6 Photocatalytic performance and mechanisms of photocatalytic enhancement

Gas phase photocatalytic reduction of CO_2 was performed on the as-synthesized TiO_2-based composites under ambient temperature and atmospheric pressure using a low-power 15 W energy-saving daylight lamp as the visible light source. During the photocatalytic reactions, CH_4 was detected as the only product in the outlet gas based on the GC analysis. Generally, the yield of CH_4 increased with the irradiation duration for all the photocatalysts. The total yield of CH_4 for 10 h of reaction was calculated and the results are summarized in Fig. 10. The photocatalytic activity of the CH_4 formation was found to follow the order: N–TiO_2-001/GR > TiO_2-001/GR > N–TiO_2/GR > TiO_2/GR>

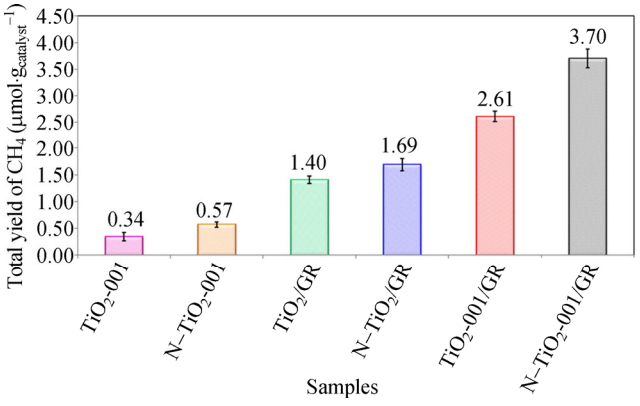

Figure 10 Total yield of CH_4 over as-synthesized TiO_2-001, N–TiO_2-001 and a series of TiO_2-based/GR nanocomposites.

N–TiO_2-001 > TiO_2-001. To understand the mechanistic pathway of CH_4 formation, a series of control experiments was conducted under the following conditions: (1) N–TiO_2-001/GR coated on the glass rods in the dark in a flow of CO_2 and H_2O vapor, (2) without loading of N–TiO_2-001/GR on the glass rods in a flow of CO_2 and H_2O vapor under light irradiation, (3) N–TiO_2-001/GR coated on the glass rods in a flow of CO_2 without H_2O vapor under light irradiation and (4) N–TiO_2-001/GR coated on the glass rods in a flow of N_2 and H_2O vapor under light irradiation. In all cases, no appreciable CH_4 was detected (Fig. S15 in the ESM). These background tests confirmed that any CH_4 formed was solely generated from the reaction of CO_2 and H_2O over the photocatalysts under visible light and certainly not from the photodecomposition of organic residues or impurities on the catalyst surface. Therefore, it can be reiterated that all three components, namely photocatalyst, reactants feed (CO_2 and H_2O) and light source are prerequisites for the photocatalytic CO_2 reduction process.

Among all the studied photocatalysts, pure TiO_2-001 exhibited the lowest efficiency for CO_2 reduction due to its limited photoresponse range in visible light, whereas N–TiO_2-001 exemplified a slight improvement in the photocatalytic activity for CH_4 production due to an additional visible light absorption shoulder formed between 400 and 550 nm. With the incurporation of ATSEG in the TiO_2-based photocatalysts, all the TiO_2-based/GR nanocomposites displayed an overall enhancement in the CH_4 evolution from the CO_2 photoconversion process. Comparing with pure TiO_2-001 and N–TiO_2-001, the higher conversion of CO_2 can be mainly attributed to several concomitant factors, which are closely related to the advantageous presence of ATSEG in the nanocomposites. Firstly, the specific surface area of TiO_2-based/GR nanocomposites was generally larger (at least 1.8 times) than that of TiO_2-based composites in the absence of ATSEG as shown in Table S2 (in the ESM). The specific surface areas of pure TiO_2-001, N–TiO_2-001, N–TiO_2/GR and N–TiO_2-001/GR were 39.8, 43.1, 88.5 and 77.4 $m^2 \cdot g^{-1}$ respectively. The higher surface areas of N–TiO_2/GR and N–TiO_2-001/GR is due to the presence of graphene, which possesses an extremely high surface area (theoretical value of 2,600 $m^2 \cdot g^{-1}$). Therefore, the high surface areas of graphene-based photocatalysts provide more active adsorption sites and photocatalytic reaction centers not only on the surface of the semiconductor catalysts, but also on the graphene sheets, allowing more reactant molecules to take part in the reaction. This greatly enlarged the reaction space to initiate the charge transfer.

Secondly, the enhanced conversion rate was due to the fact that the d-orbitals of TiO_2-based match well with the π-orbital of ATSEG in energy level, forming d–π electron orbital overlap. This led to strong Ti–O–C bonds in the nanocomposites as shown by the XPS and FTIR results. This can be expected to promote interfacial charge carrier transfer in the hybrid heterostructures. One photon usually induces the transfer of only one electron in photochemical reactions. Nevertheless, CO_2 reduction requires an 8-electron process to yield CH_4. Upon visible light illumination, the excited state of electrons, transported from the TiO_2-based composites to the ATSEG via a percolation mechanism, was shuttled freely along the conducting network of ATSEG which retards the recombination of charge carriers by facilitating the separation of electron–hole pairs [51]. Subsequently, these photo-induced electrons transferred to the surface and reacted with CO_2. In the absence of ATSEG, most of these charges tend to recombine rapidly without undergoing any reactions. This is principally due to the adsorption kinetics of the CO_2 molecules (10^{-8}–10^{-3} s) on the nanocomposites being slower than the electron–hole recombination time (10^{-9} s) [9, 18].

Furthermore, when visible light was irradiated on

the surface of TiO_2-based/GR nanocomposites, the ATSEG enhanced the visible light absorption and reduced the reflection of light since it served as a sensitizer, which is in essence similar to our previous study of the use of CNT-based composites for the improvement of visible light absorption [13]. When integrated with ATSEG, the nanocomposites showed an obvious red shift in the absorption edge with reduced band gap energies and higher absorption intensity in the visible region (Fig. 9), suggesting that the incorporation of ATSEG is of utmost importance for the absorption of visible light to initiate the charge transfer process. More importantly, the low number of defects in the ATSEG scaffold, as confirmed by Raman analysis (Fig. 7(b)), endows ATSEG with improved electrical mobility and a longer electronic mean free path so that energetic electrons are delocalized over a large area of the 2D planar structure of ATSEG surface. In this way, the likelihood of interaction with the adsorbed CO_2 was substantially boosted due to the decreased rate of recombination of charge carriers on light irradiation.

By comparing all the TiO_2-based/GR photocatalysts, it was found that the photocatalytic activity of N–TiO_2/GR was greater than that of TiO_2/GR. This is ascribed to the presence of localized states created by N-doping modifying the electronic band structure of TiO_2 allowing a greater utilization of visible light [52]. This is also further proven by the PL spectra (Fig. 11), which indicate a much lower recombination rate of charge carriers in N–TiO_2/GR nanocomposites than that in TiO_2/GR. Moreover, N–TiO_2-001/GR exhibited the best photo-activity in the CO_2 reduction with the highest CH_4 yield of 3.70 $\mu mol \cdot g_{catalyst}^{-1}$ being recorded, compared to that of TiO_2-001/GR (2.61 $\mu mol \cdot g_{catalyst}^{-1}$), N–$TiO_2$/GR (1.69 $\mu mol \cdot g_{catalyst}^{-1}$) and N–$TiO_2$-001 (0.57 $\mu mol \cdot g_{catalyst}^{-1}$) under visible illumination. This agreed well with the PL results (Fig. 11), in which the weakest PL peak is observed for N–TiO_2-001/GR photocatalysts. Similar findings due to the localized states of N-doping could be evidenced for a higher CH_4 yield in N–TiO_2-001/GR than that in TiO_2-001/GR. Following the significantly enhanced photocatalytic activity, the apparent quantum yield of N–TiO_2-001/GR was measured to be approximately 0.0603% (see Table S3 in the ESM for detailed calculations).

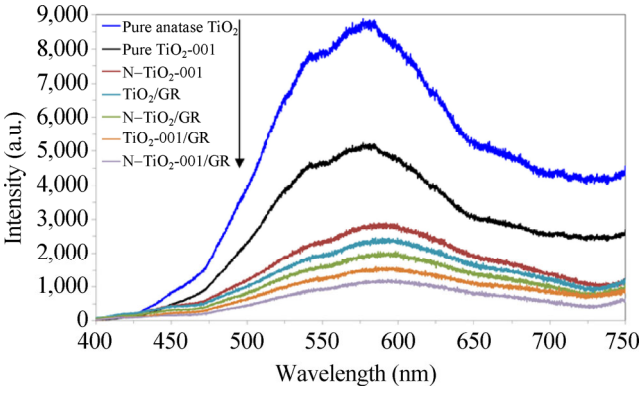

Figure 11 PL spectra of pure anatase TiO_2, pure TiO_2-001, N–TiO_2-001, TiO_2/GR, N–TiO_2/GR, TiO_2-001/GR and N–TiO_2-001/GR nanocomposites.

As mentioned earlier, an efficient charge separation and transfer are essential for increasing the photocatalytic activity. It is known that the separation of photogenerated electron–hole pairs is also accelerated by the presence of {001} facets besides the role of ATSEG [26]. This is because {001} facets are regarded as oxidation sites for the photooxidation process whereas {101} facets offer reduction sites for the photoreduction process which act as reservoirs of photogenerated electrons [53]. Apart from that, theoretical and experimental studies have demonstrated that the {001} facets of TiO_2 are more reactive than the thermodynamically stable {101} surface [7], which could be one of the primary reasons for the enhancement of CO_2 reduction to CH_4. This agrees very well with our experimental results (CH_4 yield: N–TiO_2-001/GR > N–TiO_2/GR) and highlights for the first time the importance of {001} facets mediated by surface fluorination in the CO_2 reduction reaction.

On the basis of the above results and discussion, a mechanism for the visible light photocatalytic reaction over N–TiO_2-001/GR nanocomposites can be proposed, as shown in Fig. 12. Briefly, N 2p of N–TiO_2-001, which is located above the VB maximum (O 2p), absorbed the visible light irradiation and excited the electrons from N 2p to the CB of N–TiO_2-001. When N–TiO_2-001 was modified by ATSEG sheets, the excited electrons on the CB of N–TiO_2-001 could be easily transferred to ATSEG sheets due to the lower Fermi level of ATSEG compared to N–TiO_2-001, resulting in the separation of electron–hole pairs and inhibition of

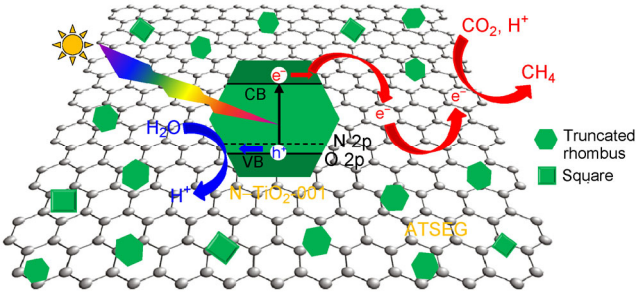

Figure 12 Schematic illustration of the charge transfer and separation of electron–hole pairs for the reduction of CO_2 with H_2O to CH_4 using N–TiO_2-001/GR nanocomposites under visible light irradiation (e^- denotes electrons and h^+ denotes holes).

the recombination of charge carriers. The enriched electron density on ATSEG favors the reduction of CO_2 to CH_4. The photocatalytic CO_2 transformation to CH_4 over N–TiO_2-001/GR nanocomposites can be explained using energy band theory. Commonly, the excited electrons can be consumed effectively if the reduction potential of the desired reaction is lower than the CB potential of the semiconductor [54]. The CB flatband potential of N–TiO_2-001 is –0.5 V vs. NHE and the reduction potential of CO_2/CH_4 (Eq. (3)) is –0.24 V vs. NHE [13]. Seeing that the CO_2/CH_4 reduction potential is less negative than the CB flatband potential, the reaction (Eq. (3)) is thermodynamically stable even though eight electrons are required to convert CO_2 to CH_4. Furthermore, the production of CH_4 is thermodynamically easier than the formation of CO because the reduction potential of CO_2/CH_4 (–0.24 V vs. NHE) is less negative than that for CO_2/CO (–0.52 V vs. NHE) [55]. Meanwhile, hydrogen (H_2) was not detected by GC. It is likely that the photogenerated H· radicals and H_2 were quickly consumed by CO_2 in the photocatalytic reaction process. Another possible explanation is that H_2 production usually requires the presence of noble metals such as Pt or Ag to reduce the overpotential in the H_2 production [55]. However, our experiment did not involve any noble metals. Similar outcomes have been reported in the literature by Li et al. [56] during photocatalytic CO_2 with H_2O vapor using TiO_2-based photocatalysts. The major reaction steps in this photocatalytic mechanism are summarized by Eqs. (3)–(5)

$$GR(8e^-) + CO_2 + 8H^+ \rightarrow GR + CH_4 + 2H_2O \quad (3)$$

$$N-TiO_2\text{-}001/GR \xrightarrow{h\upsilon} GR(e^-) + N-TiO_2\text{-}001\,(h^+_{VB}) \quad (4)$$

$$N-TiO_2\text{-}001\,(2h^+_{VB}) + H_2O \rightarrow N-TiO_2\text{-}001 + 2H^+ + \frac{1}{2}O_2 \quad (5)$$

In order to provide further evidence to support the proposed photocatalytic mechanism and also elucidate the role of {001} facets, N-doping and ATSEG in the TiO_2-based photocatalytic system, PL spectral analysis (Fig. 11) was employed to study the efficiency of charge carrier trapping and recombination in the TiO_2-based/GR nanocomposites. The PL spectra of the TiO_2-based/GR nanocomposites are similar to that of pure anatase TiO_2 which has a strong emission peak at ca. 580 nm. In particular, the PL peak emission intensity was found to follow the order: Pure anatase TiO_2 > pure TiO_2-001 > N–TiO_2-001 > TiO_2/GR > N–TiO_2/GR > TiO_2-001/GR > N–TiO_2-001/GR. The PL intensity of pure TiO_2-001 was lower than that of pure anatase TiO_2 with predominantly {101} facets. This is attributed to the efficient separation of photogenerated electron–hole pairs in the TiO_2-001 crystals, driving the electrons and holes to attain the most stable energy configuration in the presence of both {001} and {101} facets. The photoexcited electrons and holes migrate to the {101} and {001} facets respectively. In addition, a higher separation efficiency of the photoinduced charge carriers was observed in N–TiO_2-001 than in TiO_2-001. This could be due to the localized states of N-dopants creating electron-trapping centers, besides inducing visible light absorption [49]. In comparison to the TiO_2-based composites without ATSEG, all the TiO_2-based/GR nanocomposites displayed a decrease in PL intensity, highlighting the importance of ATSEG in reducing the recombination rate of electrons and holes leading to improved activity.

Notably, the N–TiO_2-001/GR exhibited the most significantly diminished PL intensity relative to pure anatase TiO_2 and other TiO_2-based/GR samples. This strongly suggests that the N–TiO_2-001/GR nanocomposite had the most efficient inhibition of charge carrier recombination. This can be ascribed to the fact that the electrons were excited from the N 2p levels above the O 2p VB to the CB of N–TiO_2-001 and then

transferred to the ATSEG sheet due to its excellent electronic conductivity, thus separating the photogenerated electron–hole pairs. Furthermore, with the cooperation of high energy {001} facets and N dopants, the charge transfer and separation were significantly enhanced in comparison to samples with predominantly {101} facets and without N-doping. Therefore, this could be one of the underlying factors why the N–TiO_2-001/GR photocatalyst possessed the highest photocatalytic performance towards CH_4 production from the CO_2 conversion under visible light. Overall, the PL spectra indicate that the synergistic effects between the highly reactive {001} facets, the incurporation of N-doping into the lattice of TiO_2 and the addition of ATSEG as a scaffold play key roles in extending the lifetime of the photogenerated charge carriers and enhancing the photocatalytic CO_2 reduction to CH_4.

4 Conclusions

We have successfully synthesized a hybrid heterostructure nanocomposite by *in situ* growth of well-faceted N–TiO_2 with exposed {001} facets onto an ATSEG support via a facile solvothermal strategy using NH_4F as the morphology-controlling agent. The as-developed N–TiO_2-001/GR nanocomposites have been demonstrated to be photocatalytically active under visible light for the reduction of CO_2 to CH_4 (with the highest CH_4 yield being 3.70 $\mu mol \cdot g_{catalyst}^{-1}$), which is 11-fold higher than that achieved using pure TiO_2-001 (0.34 $\mu mol \cdot g_{catalyst}^{-1}$). Interestingly, we demonstrated that our photocatalysts were active even under irradiation by low-power 15 W energy-saving light bulbs in contrast to the most widely used high-power halogen and xenon arc lamps. On the basis of FESEM, HRTEM, Raman, UV–Vis and PL spectra analyses, the high photocatalytic activity can be attributed to four main factors: (1) The formation of Ti–O–C chemical bonds resulting in a Schottky barrier at the interface between ATSEG and N–TiO_2-001, which promotes efficient charge transfer and separation, thus suppressing the recombination of electron–hole pairs. (2) The addition of ATSEG induced higher absorption intensity in the visible light region than that observed for the TiO_2-based composites in the absence of ATSEG, resulting in more efficient utilization of the solar spectrum. (3) The effective exposure of highly reactive {001} facets of N–TiO_2-001 on the ATSEG sheets facilitated a better platform for photoreduction of CO_2 to CH_4 as compared to the thermodynamically stable {101} facets. (4) The incorporation of localized states of N-dopants favored the visible light absorption as well as giving electron-trapping centers which further inhibit the recombination process. On-going research is dedicated to developing more complex graphene-based semiconducting materials in order to enhance the CH_4 yield of the CO_2 reduction process. In short, this work highlights the key significance of rational engineering of graphene-based nanocomposites by coupling graphene with semiconductors to give the next generation photocatalyst systems, and has great potential to significantly improve the photocatalytic activity and address current and future energy and environment-related issues. This work will provide new inroads into the exploration and utilization of robust graphene-based nanocomposites in order to harness both the superior electron conductivity of graphene and the high energy of {001} facets of TiO_2-based materials for the conversion of solar to chemical energy via green and sustainable photocatalysis.

Acknowledgements

This work was funded by the Ministry of Education (MOE) Malaysia under the Long-Term Research Grant Scheme (No. 2110226-113-00) and Fundamental Research Grant Scheme (No. FRGS/1/2013/TK05/MUSM/02/1).

Electronic Supplementary Material: Supplementary material (light spectrum of the low-power 15 W energy-saving daylight lamp, calculation of percentage of exposed {001} facets, FESEM images, XRD patterns and FTIR spectra of the studied photocatalysts, UV–Vis spectra of TiO_2/GR and N–TiO_2/GR, high resolution XPS spectrum of N 1s and TGA plot of N–TiO_2-001/GR nanocomposites, control experiments, and apparent quantum yield calculation) is available in the online version of this article at http://dx.doi.org/10.1007/s12274-014-0514-z.

References

[1] Hsu, H. C.; Shown, I.; Wei, H. Y.; Chang, Y. C.; Du, H. Y.; Lin, Y. G.; Tseng, C. A.; Wang, C. H.; Chen, L. C.; Lin, Y. C.; Chen, K. H. Graphene oxide as a promising photocatalyst for CO_2 to methanol conversion. *Nanoscale* **2013**, *5*, 262–268.

[2] Liou, P. Y.; Chen, S. C.; Wu, J. C. S.; Liu, D.; Mackintosh, S.; Maroto-Valer, M.; Linforth, R. Photocatalytic CO_2 reduction using an internally illuminated monolith photoreactor. *Energy Environ. Sci.* **2011**, *4*, 1487–1494.

[3] Habisreutinger, S. N.; Schmidt-Mende, L.; Stolarczyk, J. K. Photocatalytic reduction of CO_2 on TiO_2 and other semiconductors. *Angew. Chem. Int. Ed.* **2013**, *52*, 7372–7408.

[4] Fujishima, A.; Honda, K. Electrochemical photolysis of water at a semiconductor electrode. *Nature* **1972**, *238*, 37–38.

[5] Varghese, O. K.; Paulose, M.; LaTempa, T. J.; Grimes, C. A. High-rate solar photocatalytic conversion of CO_2 and water vapor to hydrocarbon fuels. *Nano Lett.* **2009**, *9*, 731–737.

[6] Linsebigler, A. L.; Lu, G.; Yates, J. T. Photocatalysis on TiO_2 surfaces: Principles, mechanisms, and selected results. *Chem. Rev.* **1995**, *95*, 735–758.

[7] Yang, H. G.; Sun, C. H.; Qiao, S. Z.; Zou, J.; Liu, G.; Smith, S. C.; Cheng, H. M.; Lu, G. Q. Anatase TiO_2 single crystals with a large percentage of reactive facets. *Nature* **2008**, *453*, 638–641.

[8] Yu, J.; Qi, L.; Jaroniec, M. Hydrogen production by photocatalytic water splitting over Pt/TiO_2 nanosheets with exposed (001) facets. *J. Phys. Chem. C* **2010**, *114*, 13118–13125.

[9] Ong, W. J.; Tan, L. L.; Chai, S. P.; Yong, S. T.; Mohamed, A. R. Facet-dependent photocatalytic properties of TiO_2–based composites for energy conversion and environmental remediation. *ChemSusChem* **2014**, *7*, 690–719.

[10] Xu, H.; Ouyang, S.; Li, P.; Kako, T.; Ye, J. High-active anatase TiO_2 nanosheets exposed with 95% {100} facets toward efficient H_2 evolution and CO_2 photoreduction. *ACS Appl. Mater. Inter.* **2013**, *5*, 1348–1354.

[11] Ong, W. J.; Tan, L. L.; Chai, S. P.; Yong, S. T.; Mohamed, A. R. Highly reactive {001} facets of TiO_2-based composites: Synthesis, formation mechanism and characterizations. *Nanoscale* **2014**, *6*, 1946–2008.

[12] Lai, Z.; Peng, F.; Wang, Y.; Wang, H.; Yu, H.; Liu, P.; Zhao, H. Low temperature solvothermal synthesis of anatase TiO_2 single crystals with wholly {100} and {001} faceted surfaces. *J. Mater. Chem.* **2012**, *22*, 23906–23912.

[13] Ong, W. J.; Gui, M. M.; Chai, S. P.; Mohamed, A. R. Direct growth of carbon nanotubes on Ni/TiO_2 as next generation catalysts for photoreduction of CO_2 to methane by water under visible light irradiation. *RSC Adv.* **2013**, *3*, 4505–4509.

[14] Park, S.; Ruoff, R. S. Chemical methods for the production of graphenes. *Nat. Nanotechnol.* **2009**, *4*, 217–224.

[15] Geim, A. K. Graphene: Status and prospects. *Science* **2009**, *324*, 1530–1534.

[16] Shen, J.; Shi, M.; Yan, B.; Ma, H.; Li, N.; Ye, M. Ionic liquid-assisted one-step hydrothermal synthesis of TiO_2–reduced graphene oxide composites. *Nano Res.* **2011**, *4*, 795–806.

[17] Zhang, Y.; Tang, Z. R.; Fu, X.; Xu, Y. J. Engineering the unique 2D mat of graphene to achieve graphene–TiO_2 nanocomposite for photocatalytic selective transformation: What advantage does graphene have over its forebear carbon nanotube? *ACS Nano* **2011**, *5*, 7426–7435.

[18] Tan, L. L.; Ong, W. J.; Chai, S. P.; Mohamed, A. R. Reduced graphene oxide–TiO_2 nanocomposite as a promising visible-light-active photocatalyst for the conversion of carbon dioxide. *Nanoscale Res. Lett.* **2013**, *8*, 465.

[19] Chen, C.; Cai, W.; Long, M.; Zhou, B.; Wu, Y.; Wu, D.; Feng, Y. Synthesis of visible-light responsive graphene oxide/TiO_2 composites with p/n heterojunction. *ACS Nano* **2010**, *4*, 6425–6432.

[20] Li, Q.; Guo, B.; Yu, J.; Ran, J.; Zhang, B.; Yan, H.; Gong, J. R. Highly efficient visible-light-driven photocatalytic hydrogen production of CdS-cluster-decorated graphene nanosheets. *J. Am. Chem. Soc.* **2011**, *133*, 10878–10884.

[21] Perera, S. D.; Mariano, R. G.; Vu, K.; Nour, N.; Seitz, O.; Chabal, Y.; Balkus Jr, K. J. Hydrothermal synthesis of graphene–TiO_2 nanotube composites with enhanced photocatalytic activity. *ACS Catal.* **2012**, *2*, 949–956.

[22] Shin, H. J.; Kim, K. K.; Benayad, A.; Yoon, S. M.; Park, H. K.; Jung, I. S.; Jin, M. H.; Jeong, H. K.; Kim, J. M.; Choi, J. Y.; Lee, Y. H. Efficient reduction of graphite oxide by sodium borohydride and its effect on electrical conductance. *Adv. Funct. Mater.* **2009**, *19*, 1987–1992.

[23] Liang, Y. T.; Vijayan, B. K.; Gray, K. A.; Hersam, M. C. Minimizing graphene defects enhances titania nanocomposite-based photocatalytic reduction of CO_2 for improved solar fuel production. *Nano Lett.* **2011**, *11*, 2865–2870.

[24] Wang, P.; Zhai, Y.; Wang, D.; Dong, S. Synthesis of reduced graphene oxide–anatase TiO_2 nanocomposite and its improved photo-induced charge transfer properties. *Nanoscale* **2011**, *3*, 1640–1645.

[25] Xiang, Q.; Lv, K.; Yu, J. Pivotal role of fluorine in enhanced photocatalytic activity of anatase TiO_2 nanosheets with dominant (001) facets for the photocatalytic degradation of acetone in air. *Appl. Catal. B* **2010**, *96*, 557–564.

[26] Ye, L.; Liu, J.; Tian, L.; Peng, T.; Zan, L. The replacement of {101} by {010} facets inhibits the photocatalytic activity of anatase TiO_2. *Appl. Catal. B* **2013**, *134–135*, 60–65.

[27] Yu, J.; Dai, G.; Xiang, Q.; Jaroniec, M. Fabrication and enhanced visible-light photocatalytic activity of carbon self-doped TiO_2 sheets with exposed {001} facets. *J. Mater. Chem.* **2011**, *21*, 1049–1057.

[28] Han, X.; Kuang, Q.; Jin, M.; Xie, Z.; Zheng, L. Synthesis of titania nanosheets with a high percentage of exposed (001) facets and related photocatalytic properties. *J. Am. Chem. Soc.* **2009**, *131*, 3152–3153.

[29] Zhang, Y.; Zhang, N.; Tang, Z. R.; Xu, Y. J. Improving the photocatalytic performance of graphene–TiO_2 nanocomposites via a combined strategy of decreasing defects of graphene and increasing interfacial contact. *Phys. Chem. Chem. Phys.* **2012**, *14*, 9167–9175.

[30] Štengl, V.; Popelková, D.; Vláčil, P. TiO_2–graphene nanocomposite as high performace photocatalysts. *J. Phys. Chem. C* **2011**, *115*, 25209–25218.

[31] Fresno, F.; Tudela, D.; Coronado, J. M.; Fernandez-Garcia, M.; Hungria, A. B.; Soria, J. Influence of Sn^{4+} on the structural and electronic properties of $Ti_{1-x}Sn_xO_2$ nanoparticles used as photocatalysts. *Phys. Chem. Chem. Phys.* **2006**, *8*, 2421–2430.

[32] Sahoo, S.; Arora, A. K.; Sridharan, V. Raman line shapes of optical phonons of different symmetries in anatase TiO_2 nanocrystals. *J. Phys. Chem. C* **2009**, *113*, 16927–16933.

[33] Lu, T.; Zhang, R.; Hu, C.; Chen, F.; Duo, S.; Hu, Q. TiO_2–graphene composites with exposed {001} facets produced by a one-pot solvothermal approach for high performance photocatalyst. *Phys. Chem. Chem. Phys.* **2013**, *15*, 12963–12970.

[34] Gu, L.; Wang, J.; Cheng, H.; Zhao, Y.; Liu, L.; Han, X. One-step preparation of graphene-supported anatase TiO_2 with exposed {001} facets and mechanism of enhanced photocatalytic properties. *ACS Appl. Mater. Inter.* **2013**, *5*, 3085–3093.

[35] Wang, W. S.; Wang, D. H.; Qu, W. G.; Lu, L. Q.; Xu, A. W. Large ultrathin anatase TiO_2 nanosheets with exposed {001} facets on graphene for enhanced visible light photocatalytic activity. *J. Phys. Chem. C* **2012**, *116*, 19893–19901.

[36] Chen, Z.; Liu, S.; Yang, M. Q.; Xu, Y. J. Synthesis of uniform CdS nanospheres/graphene hybrid nanocomposites and their application as visible light photocatalyst for selective reduction of nitro organics in water. *ACS Appl. Mater. Inter.* **2013**, *5*, 4309–4319.

[37] Sun, L.; Zhao, Z.; Zhou, Y.; Liu, L. Anatase TiO_2 nanocrystals with exposed {001} facets on graphene sheets via molecular grafting for enhanced photocatalytic activity. *Nanoscale* **2012**, *4*, 613–620.

[38] Wu, J. M.; Tang, M. L. One–pot synthesis of N–F–Cr–doped anatase TiO_2 microspheres with nearly all-(001) surface for enhanced solar absorption. *Nanoscale* **2011**, *3*, 3915–3922.

[39] Xiang, Q.; Yu, J.; Wang, W.; Jaroniec, M. Nitrogen self-doped nanosized TiO_2 sheets with exposed {001} facets for enhanced visible-light photocatalytic activity. *Chem. Commun.* **2011**, *47*, 6906–6908.

[40] Xiang, Q.; Yu, J.; Jaroniec, M. Nitrogen and sulfur co-doped TiO_2 nanosheets with exposed {001} facets: Synthesis, characterization and visible-light photocatalytic activity. *Phys. Chem. Chem. Phys.* **2010**, *13*, 4853–4861.

[41] Zhao, L.; Chen, X.; Wang, X.; Zhang, Y.; Wei, W.; Sun, Y.; Antonietti, M.; Titirici, M. M. One-step solvothermal synthesis of a carbon@TiO_2 dyade structure effectively promoting visible-light photocatalysis. *Adv. Mater.* **2010**, *22*, 3317–3321.

[42] Liu, H.; Wu, Y.; Zhang, J. A new approach toward carbon-modified vanadium-doped titanium dioxide photocatalysts. *ACS Appl. Mater. Inter.* **2011**, *3*, 1757–1764.

[43] Xiang, Q.; Yu, J.; Jaroniec, M. Enhanced photocatalytic H_2-production activity of graphene-modified titania nanosheets. *Nanoscale* **2011**, *3*, 3670–3678.

[44] Tu, W.; Zhou, Y.; Liu, Q.; Yan, S.; Bao, S.; Wang, X.; Xiao, M.; Zou, Z. An *in situ* simultaneous reduction–hydrolysis technique for fabrication of TiO_2–graphene 2D sandwich-like hybrid nanosheets: Graphene-promoted selectivity of photocatalytic-driven hydrogenation and coupling of CO_2 into methane and ethane. *Adv. Funct. Mater.* **2013**, *23*, 1743–1749.

[45] Liu, G.; Yang, H. G.; Wang, X.; Cheng, L.; Pan, J.; Lu, G. Q.; Cheng, H. M. Visible light responsive nitrogen doped anatase TiO_2 sheets with dominant {001} facets derived from TiN. *J. Am. Chem. Soc.* **2009**, *131*, 12868–12869.

[46] Liu, G.; Sun, C.; C. Smith, S.; Wang, L.; Lu, G. Q.; Cheng, H. M. Sulfur doped anatase TiO_2 single crystals with a high percentage of {001} facets. *J. Colloid Interf. Sci.* **2010**, *349*, 477–483.

[47] Liu, G.; Wang, L.; Sun, C.; Yan, X.; Wang, X.; Chen, Z.; Smith, S. C.; Cheng, H. M.; Lu, G. Q. Band-to-band visible-light photon excitation and photoactivity induced by homogeneous nitrogen doping in layered titanates. *Chem. Mater.* **2009**, *21*, 1266–1274.

[48] Zhang, N.; Zhang, Y.; Pan, X.; Fu, X.; Liu, S.; Xu, Y. J. Assembly of CdS nanoparticles on the two-dimensional graphene scaffold as visible-light-driven photocatalyst for selective organic transformation under ambient conditions. *J. Phys. Chem. C* **2011**, *115*, 23501–23511.

[49] Yu, J.; Li, Q.; Liu, S.; Jaroniec, M. Ionic-liquid-assisted synthesis of uniform fluorinated B/C-codoped TiO_2 nanocrystals and their enhanced visible-light photocatalytic activity. *Chem.—Eur. J.* **2013**, *19*, 2433–2441.

[50] Zhang, J.; Wu, Y.; Xing, M.; Leghari, S. A. K.; Sajjad, S.

Development of modified N doped TiO_2 photocatalyst with metals, nonmetals and metal oxides. *Energy Environ. Sci.* **2010**, *3*, 715–726.

[51] Lv, X. J.; Zhou, S. X.; Zhang, C.; Chang, H. X.; Chen, Y.; Fu, W. F. Synergetic effect of Cu and graphene as cocatalyst on TiO_2 for enhanced photocatalytic hydrogen evolution from solar water splitting. *J. Mater. Chem.* **2012**, *22*, 18542–18549.

[52] Wang, D. H.; Jia, L.; Wu, X. L.; Lu, L. Q.; Xu, A. W. One-step hydrothermal synthesis of N-doped TiO_2/C nanocomposites with high visible light photocatalytic activity. *Nanoscale* **2012**, *4*, 576–584.

[53] Roy, N.; Sohn, Y.; Pradhan, D. Synergy of low-energy {101} and high-energy {001} TiO_2 crystal facets for enhanced photocatalysis. *ACS Nano* **2013**, *7*, 2532–2540.

[54] Tahir, M.; Amin, N. S. Photocatalytic reduction of carbon dioxide with water vapors over montmorillonite modified TiO_2 nanocomposites. *Appl. Catal. B* **2013**, *142–143*, 512–522.

[55] Yu, J.; Jin, J.; Cheng, B.; Jaroniec, M. A noble metal-free reduced graphene oxide–CdS nanorod composite for the enhanced visible-light photocatalytic reduction of CO_2 to solar fuel. *J. Mater. Chem. A* **2014**, *2*, 3407–3416.

[56] Li, X.; Zhuang, Z.; Li, W.; Pan, H. Photocatalytic reduction of CO_2 over noble metal-loaded and nitrogen-doped mesoporous TiO_2. *Appl. Catal. A* **2012**, *429–430*, 31–38.